

Article

The Characterization and SCR Performance of Mn-Containing α -Fe₂O₃ Derived from the Decomposition of Siderite

Fuwei Sun ^{1,2}, Haibo Liu ^{1,2,*}, Daobing Shu ^{1,2}, Tianhu Chen ^{1,2} and Dong Chen ^{1,2}

¹ Key Laboratory of Nano-minerals and Pollution Control of Anhui Higher Education Institutes, Hefei University of Technology, Hefei 230009, China

² Institute of Environmental Minerals and Materials, School of Resources and Environmental Engineering, Hefei University of Technology, Hefei 230009, China

* Correspondence: liuhaibosky116@hfut.edu.cn

Received: 6 May 2019; Accepted: 24 June 2019; Published: 28 June 2019



Abstract: In this work, a nano-structured iron-manganese oxide composite was prepared by calcining natural manganese-rich siderite at different temperatures (450, 500, 550, 600 °C, labeled as H450, H500, H550, H600, respectively), and their performances of selective catalytic reduction (SCR) of NO by NH₃ were investigated. XRD, XRF, BET, XPS, SEM, and TEM were used to investigate the morphology, composition, and surface characteristics of the catalyst. The results showed that the decomposition of siderite occurred from 450 °C to around 550 °C during the calcination in air atmosphere; moreover, the siderite could be converted into nano-structured α -Fe₂O₃. The specific surface area of the material increased, and Mn²⁺ was transformed into Mn⁴⁺, which were beneficial to the SCR. Among these catalysts, H550 had the best SCR performance, with NO removal of 98% at a temperature window from 200 to 250 °C. The presence of water vapor and sulfur dioxide can inhibit the SCR performance of the catalysts, but this inhibition effect was not obvious for H550 at the optimum reaction temperature (250 °C). The findings presented in this study are significant toward the application of the Mn-rich siderite as a precursor in preparing the Fe-Mn oxides for catalytic de-NO_x by SCR.

Keywords: siderite; thermal treatment; nanostructurization; SCR

1. Introduction

Nitrogen oxides (NO_x) emitted from various sources are a major atmospheric pollutant, causing acid rain, photochemical smog, and endangering human health and the ecological environment [1–4]. The world energy infrastructure being based on fossil energy further aggravates NO_x pollution to a certain extent. Many technical methods have been purposed for controlling nitrogen oxides, of which selective catalytic reduction (SCR) for NO removal with NH₃ has been the most investigated technology for several decades [5–8], especially low-temperature SCR [9]. For the catalysts, TiO₂-supported vanadium-based catalysts such as V₂O₅–WO₃/TiO₂ catalysts are widely used due to their advantages, including high NO conversion, N₂ selectivity, resistance to sulfur toxicity, and strong mechanical strength [10–13]. However, considering the high reaction temperature and environmental toxicity of vanadium-based catalysts [14–16], vanadium-free catalysts like metal oxides (Fe, Mn, Cu, Ce) have received more and more attention [17–19].

Iron oxides and manganese oxides are preferred as vanadium-free catalysts due to their good low-temperature activity and high NO conversion. In previous studies, α -Fe₂O₃ was shown to have outstanding SCR performance in the temperature range 200–400 °C [20]. Moreover, studies have shown that calcined siderite can form nano-scale α -Fe₂O₃, accompanied during the transformation process by the phases FeCO₃–Fe₃O₄– γ -Fe₂O₃– α -Fe₂O₃ [21]. Meanwhile, manganese oxides are generally used as

an active component supported on a carrier. Common examples including $\text{MnO}_x\text{-CeO}_2/\text{CNTs}$ and Mn-Fe/TiO_2 have excellent SCR activity [22–24].

On the other hand, siderite is abundant in China with a low utilization rate [25,26]. Calcined siderite can form Fe_2O_3 and Fe_3O_4 [27]. The calcination process can increase the specific surface area still [28], and the calcined product is an environmentally friendly and highly active mineral material [27,29]. Additionally, the substitution of Mn for Fe in the structure of naturally occurring siderite is universal. Moreover, the presence of manganese oxides can improve the low temperature activity of a catalyst [30]. Thus, Fe–Mn oxides with abundant micropores and large specific surface areas should be obtained by the thermal decomposition of siderite.

In this present study, natural Mn-rich siderite was used to prepare Fe–Mn oxides with abundant micropores for SCR evaluation. The effects of calcination temperature on the material and SCR activity of the catalysts were investigated by the laboratory-scale catalytic system. The samples were characterized by X-ray Diffraction (XRD), X-ray Photoelectron Spectroscopy (XPS), Raman, Scanning Electron Microscope (SEM), Transmission Electron Microscope (TEM), and Brunauer-Emmett-Teller (BET). The objectives of the present work were (i) to obtain an iron-manganese oxide catalyst by calcining siderite, (ii) to investigate the effects of calcination temperature and various parameters (such as water vapor and sulfur) on the SCR reaction, and (iii) to examine the relationship between the structure of calcined products and SCR performance.

2. Experimental Methods

2.1. Catalyst Preparation

Natural siderite was collected from Rushan, Shandong Province, China. The sample was separated by a 40–60 mesh standard sieve after grinding and crushing. Afterwards, four groups of the catalysts were prepared by calcining in muffle furnace for 1 h at different temperatures (450, 500, 550, 600 °C) and labeled as H450, H500, H550, H600, respectively.

2.2. Catalyst Characterization

Crystal phases of the samples were determined by using a Dandong DS-2700 X-ray diffractometer ($\text{Cu K}\alpha$, with 2θ ranging between 5° and 70° and operated at 40 KV and 30 mA). Determination of the decomposition temperature was carried out using a thermogravimetric analyzer (EXSTAR S II TG/DTG7300, Hitachi, Tokyo, Japan). An X-ray photoelectron spectrometer (Thermo ESCALAB250Xi, ThermoFisher, Waltham, MA, USA) was used to analyze the elemental distribution and valence state of the catalysts. A scanning electron microscope (SEM, SU8020, Hitachi, Tokyo, Japan) and a transmission electron microscope (TEM, JEM-2100F, JEOL, Tokyo, Japan) were used to characterize the morphology of the samples. The molecular structures of samples were analyzed by Raman spectroscopy using an HR Evolution Raman spectrometer from HORIBA (Jobin Yvon, Paris, France). Chemical composition was measured on an X-ray fluorescence spectrometer (Shimadzu XRF-1800, Shimadzu, Kyoto, Japan) with Rh radiation. The specific surface area, pore volume, and pore size distribution of the samples were analyzed using a surface area and pore size analyzer (Quanta NOVA 3000e, Quantachrome, Shanghai, China).

2.3. Catalytic Activity Testing

The SCR evaluation of the as-prepared catalysts was carried out by fixing the catalyst volume in a quartz tube reactor with an inner diameter of 6 mm. The simulated flue gas was controlled by mass flow controllers at a flow rate of $150 \text{ mL}\cdot\text{min}^{-1}$ (including the carrier gas (Ar), 500 ppm of NH_3 , 500 ppm of NO, and 1.5% of O_2). The reaction temperature ranged from 50 to 400 °C with a gas hourly space velocity (GHSV) of 16000 h^{-1} . When the SCR reaction was stable, the concentrations of the outlet gases were detected by a flue gas analyzer (C500, ONUEE, Shenzhen, China). The experimental setup involving gas mixing system, reaction system, and detecting system is shown in Figure 1.

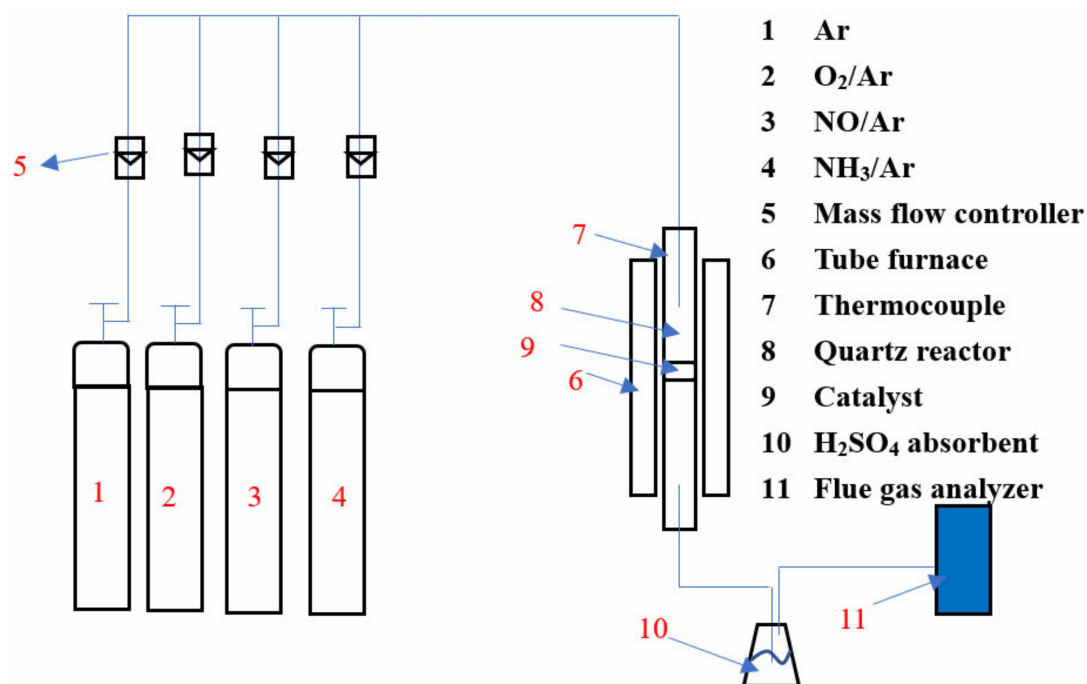


Figure 1. The experimental setup for selective catalytic reduction (SCR) evaluation.

NO conversion is calculated by the following Equation (1):

$$\text{NO conversion} = \frac{[\text{NO}]_{\text{in}} - [\text{NO}]_{\text{out}}}{[\text{NO}]_{\text{in}}} \times 100\% \quad (1)$$

3. Results and Discussion

3.1. XRD, XRF, and TG of Siderite before and after Calcination

Figure 2b shows the TG and DTG results of the natural siderite calcined in air atmosphere from 20 to 800 °C with a heating rate of 10 °C/min. According to previous studies, the main decomposition of siderite started at 478 °C and ended at 580 °C, with a maximum rate at 529 °C [31]. In this experiment, the natural siderite was almost in a stable state with a mass loss of roughly 1.13% before 400 °C. Then, a significant mass loss of approximately 30.94% occurred from 420 to 600 °C, which should be ascribed to the decomposition of siderite (FeCO₃) into Fe₂O₃ [32]. According to the TG/DTG results, the calcination temperatures of 450, 500, 550, and 600 °C were selected for catalyst preparation.

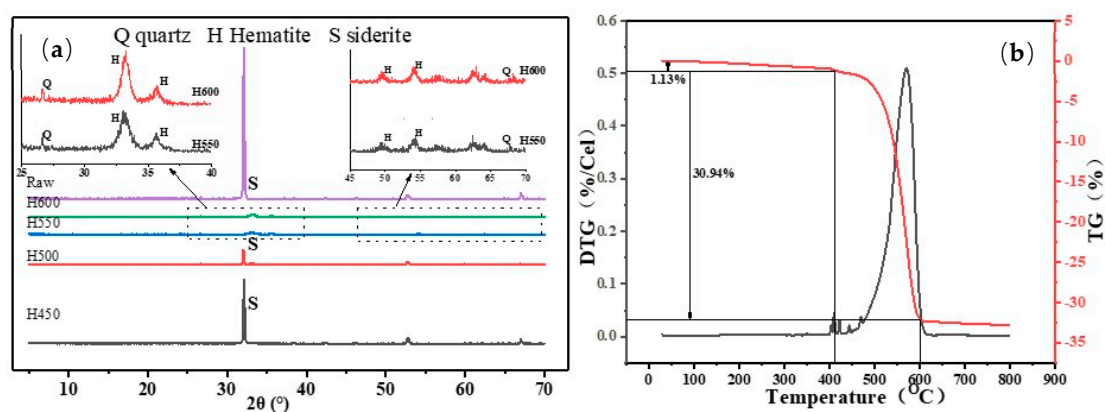


Figure 2. XRD patterns of siderite before and after thermal treatment (a); TG and DTG profiles of siderite (b).

The XRD patterns of the natural siderite and thermally treated samples are shown in Figure 2a. Combined with the standard cards (JCPD77-1060, JCPD12-531, JCPD86-2368), it was concluded that the natural siderite was mainly composed of FeCO_3 with a small amount of quartz. The reflections of quartz and FeCO_3 were observed at $2\theta = 22.6^\circ, 32.08^\circ, 42.68^\circ, 52.72^\circ$ and 51.08° , respectively. The reflections of FeCO_3 disappeared while the reflections of Fe_2O_3 could be observed at $2\theta = 33.1^\circ, 35.6^\circ, 54.3^\circ$, and 62.4° when the calcination was over 550°C , indicating the complete decomposition of siderite (FeCO_3) to hematite ($\alpha\text{-Fe}_2\text{O}_3$). The change to iron oxide was very obvious based on the XRD pattern, while the change to manganese oxide was not. This may be due to low content of manganese oxide or the substitution of Mn for Fe in the structure of the siderite [10].

The XRF results show that the sample was composed of Fe_2O_3 (58.995 wt %), MnO (3.46 wt %), SiO_2 (1.73 wt %), and traces of CaO and MgO, with an ignition loss of about 32.5%. According to previous studies, the existence of manganese oxides had favorable effect for the SCR reactions [33,34]. Therefore, the confirmation of the valence of Mn will be carried out in the next section.

3.2. XPS

XPS analysis was conducted to identify the species on the surface of the natural siderite and thermally treated samples. According to the XRD patterns, the distinct peak at about 711.0 eV belonged to Fe^{3+} [35,36], as shown in Figure 3a. The peaks for Fe^{2+} and FeCO_3 were detected at around 709 and 713 eV, respectively [37,38]. The peaks of FeCO_3 experienced an obvious decrease as the calcination temperature increased to 450°C and were then replaced by the characteristic peak of Fe^{3+} as the temperature reached 500°C [39]. This also proved that the increasing temperature favored the decomposition of siderite, especially for the temperature of 550°C .

As displayed in Figure 3c, the peaks at the binding energy of 530 and 532 eV were assigned to the lattice oxygen O^{2-} (denoted as O_β) and the surface-adsorbed oxygen (denoted as O_α), respectively [40]. As the calcination temperature increased to 500°C , the intensity of O_β was gradually enhanced, while the intensity of O_α became weaker. Interestingly, this variation exhibited an opposite trend when the calcination temperature further increased to 600°C . It was reported that O_α was more beneficial for the SCR reactions via a “fast SCR” process because of its higher mobility [41]. The $\text{O}_\alpha/(\text{O}_\alpha + \text{O}_\beta)$ ratio was the lowest in the case of H550, but O_α still occupied the main part, with 60.5%. Therefore, it is believed the thermal treatment products will have a good SCR performance.

To the best of our knowledge, Mn^{4+} species were considered as the active sites for SCR reactions. Previous studies have shown that Mn^{4+} , Mn^{3+} , and Mn^{2+} often existed in material [33,42]. Therefore, the distribution of the Mn valence was determined. As presented in Figure 3b, the peaks at 641.2 and 642.6 eV were attributed to Mn^{3+} and Mn^{4+} , respectively [36,43]. The peaks near 640.8 and 641.7 eV were attributed to Mn^{2+} and Mn^{3+} , respectively [7,23]. Other XPS peaks were attributed to Mn^{4+} at a binding energy of around 642.8 eV [44,45]. It can be deduced from Figure 3 that with an increase in calcination temperature to 500°C , the Mn^{4+} on the surface increased gradually. When the calcination temperature attained 550°C , a large amount of Mn^{4+} is formed accompanied by a small amount of Mn^{3+} . As the temperature increased to 600°C , the content of Mn^{4+} decreased, which is not conducive to SCR performance [7].

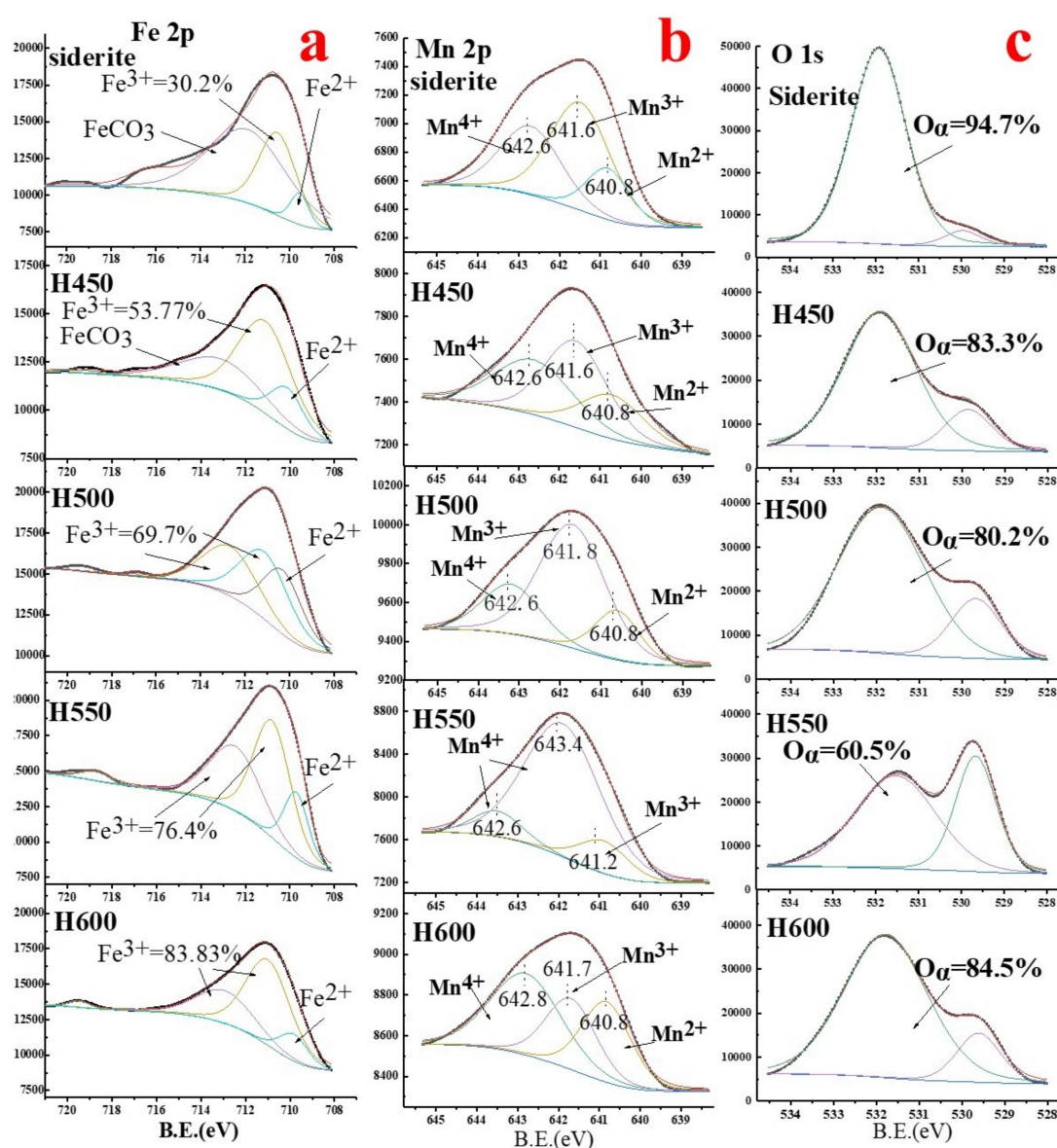


Figure 3. XPS spectra of Fe 2p (a), O 1s (b), and Mn 2p (c) of the natural siderite and thermally treated samples.

3.3. SEM and TEM

The SEM images of the natural siderite and thermally treated samples are displayed in Figure 4. The bulk siderite with a relatively even and smooth surface can be observed in Figure 4a [46]. Moreover, there were much fewer siderite aggregated particles with irregular shape on the surface of the bulk siderite [47]. With an increase in the calcination temperature, the bulk siderites were cleaved into small grains, and the surfaces of H500 (Figure 4b), H550 (Figure 4c), and H600 (Figure 4d) became loose. In addition, almost no pores can be observed in the structure of the natural siderite, as shown in Figure 4e. The EDX also confirmed the existence of Mn oxide in the siderite. However, numerous nanopores with diameters of 10 to 20 nm appeared in H550 (Figure 4f). Based on the XRD results, siderite was completely decomposed into hematite, and a large amount of carbon dioxide was produced during the calcination process at 550 °C. Thus, the formation of these nanopores was related to the decomposition of siderite. It was reported that the property of the nanoporous structure was beneficial for SCR reactions [7]. As shown in Figure 4e,f, the EDX elemental mapping images of Mn and Fe demonstrated that the distribution of Mn was partially overlapped with that of Fe. This phenomenon

was probably due to the substitution of Mn for Fe in the structure of the siderite, since the isomorphous substitution of Mn for Fe is a universal occurrence in the natural siderite [48].

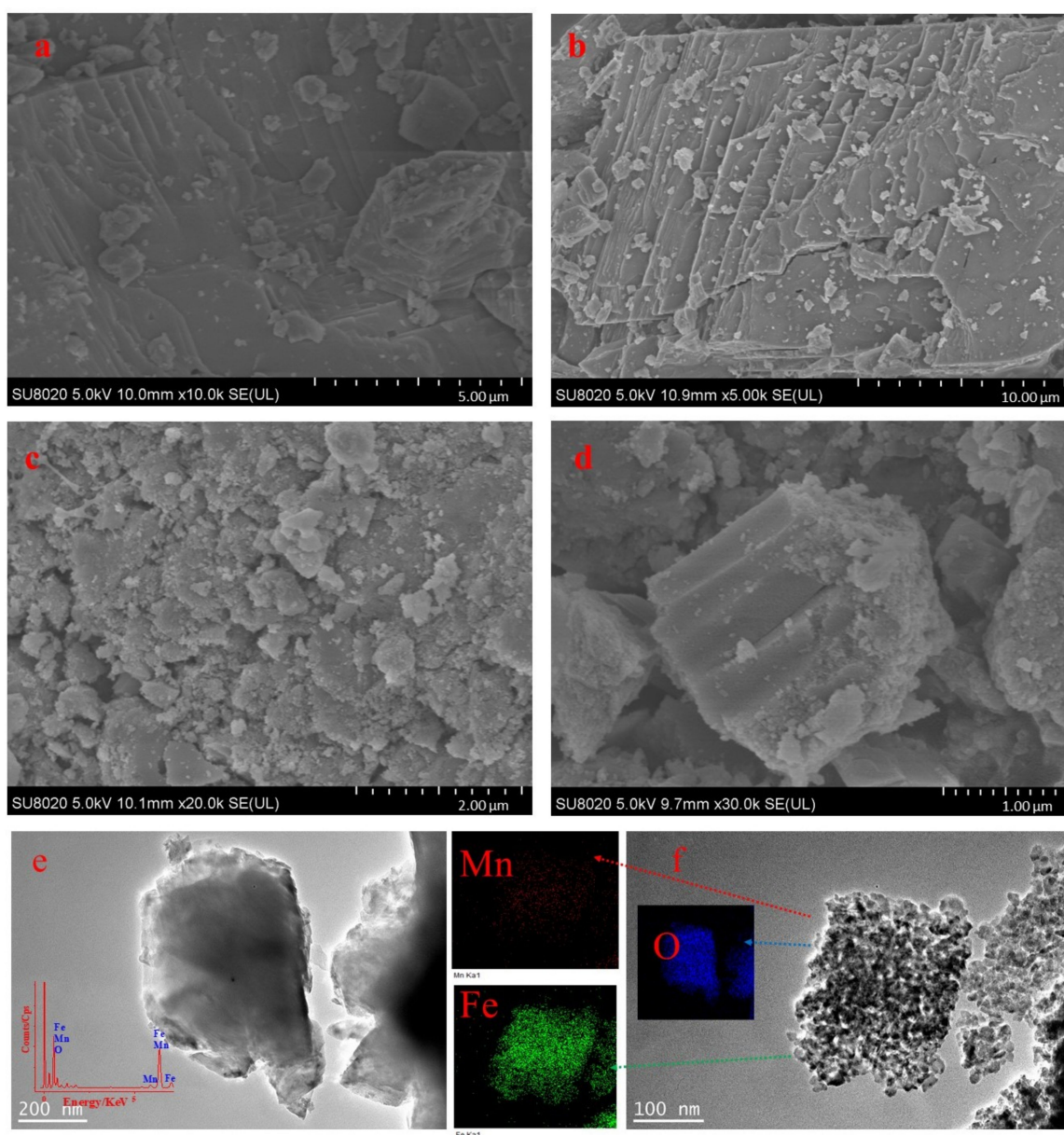


Figure 4. SEM images of (a) the natural siderite, (b) H500, (c) H550, and (d) H600, and TEM images of (e) the natural siderite, (f) H550.

3.4. BET and Raman

The BET specific surface area (BET-SSA), pore volume, and pore size are displayed in Table 1. The order of BET-SSA was as follows: H550 ($54.99 \text{ m}^2 \cdot \text{g}^{-1}$) > H500 ($52.04 \text{ m}^2 \cdot \text{g}^{-1}$) > H600 ($37.26 \text{ m}^2 \cdot \text{g}^{-1}$) > H450 ($14.1 \text{ m}^2 \cdot \text{g}^{-1}$), indicating the thermal treatment significantly affected the specific surface area of the samples. As is well known, catalysts with a large specific surface area are beneficial to the catalytic reaction due to the greater number of active sites [5].

The N_2 adsorption-desorption isotherms and pore size distributions of H450, H500, H550, and H600 are shown in Figure 5a. In general, the isotherms of the samples exhibited a type IV isotherm, suggesting that the prepared samples were typical mesoporous materials [49]. The pore sizes of these samples were in the range 2–20 nm. These mesopores should provide more internal specific surface

area and pore volume promoting the SCR efficiency [14]. According to the XRD, SEM, and TEM results, the decomposition of FeCO_3 and escape of CO_2 should be taken into consideration for the formation of nanoparticles and pore structures. A rich mesoporous structure allows the material to be more accessible to the reactant gases [50].

Raman spectroscopy was used to further analyse the molecular structure of the active element component in this study and the results are presented in Figure 5b. According to previous studies, the bands appearing at 182, 282, 734, and 1084 cm^{-1} were assigned to siderite [51,52]. After calcination, some new bands at 220, 288, 404, 608, and 652 cm^{-1} were found and identified as hematite ($\alpha\text{-Fe}_2\text{O}_3$) [53]. It was reported that the band around 650 cm^{-1} was not a perfect spectrum of hematite ($\alpha\text{-Fe}_2\text{O}_3$) [54]. Some studies have found that the bands near 580–650 cm^{-1} can also be assigned to MnO_2 [55,56]. Therefore, the band at 650 cm^{-1} could also be ascribed to MnO_2 [10]. This was consistent with the XPS results.

Table 1. Specific surface area, pore volume, and average pore size of H450–H600.

Sample	BET-SSA (m^2/g)	Pore Volume(cc/g)	Average Pore Size(nm)
H450	14	0.028	8.069
H500	52	0.087	6.661
H550	54	0.152	11.033
H600	37	0.147	15.78

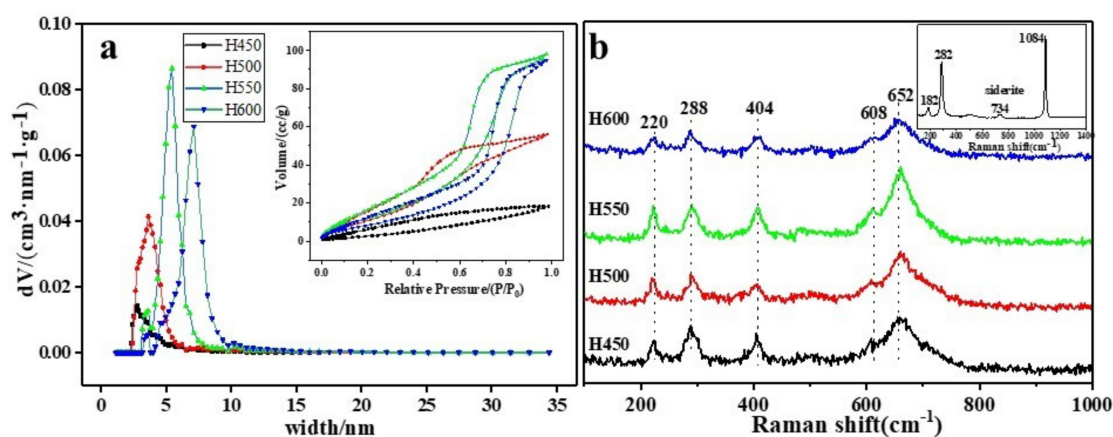


Figure 5. N_2 adsorption-desorption isotherms and pore size distributions (a) and Raman spectra (b) of the different samples.

3.5. SCR Performance and Resistance

The SCR activities of the as-prepared samples were examined in terms of the NO conversions under different reaction temperatures. It was noted that siderite exhibited very low SCR activity, with about 20% NO conversion (Figure 6a). However, the SCR performance was greatly enhanced after calcination at different temperatures. NO conversion of 64% was obtained for H450 at 250 $^\circ\text{C}$, nearly 100% for H500 and H550 at 200–250 $^\circ\text{C}$, and 95% for H600 at 250 $^\circ\text{C}$, respectively. The relatively low SCR activities of H450 and H600 could be due to the low specific surface area and lattice oxygen content. In addition, the thermally treated Mn-rich siderite (H500 and H550) had a lower reaction temperature window compared with that of the common $\alpha\text{-Fe}_2\text{O}_3$ (250–300 $^\circ\text{C}$) [40]. This phenomenon could be ascribed to the oxidization of MnCO_3 to MnO_2 during the calcination process, which greatly enhanced the low temperature activity of the material. However, the NO conversion gradually decreased when the reaction temperature was over 250 $^\circ\text{C}$, which was likely caused by the NH_3 oxidation at high temperatures. In summary, large specific surface area and porous structure, the existence of MnO_2 , and the particular adsorption state of oxygen improved for the SCR performance of the newly formed $\alpha\text{-Fe}_2\text{O}_3$ [14,57].

According to the literature [34], the content of water vapor in the flue gas is approximately 6 to 12%. Therefore, it is necessary to evaluate the SCR performance of the samples under the existence water vapor. As shown in the Figure 6b, NO conversions of H550 under different contents of water vapor showed an obvious decline in the range 150–250 °C, indicating the addition of water vapor had a certain influence on the SCR activity. It was reported that the presence of water vapor would lead to the transformation of Lewis acid to Brønsted acid [58]. This is also the reason why many studies have shown that the effect on SCR is reversible when relieving water vapor [24,59]. Comparing different water vapor concentrations in H550 catalytic treatment of NO, the higher the concentration of water vapor, the more obvious the activity inhibition at low temperature. However, the effect of water vapor gradually decreases with the increase of reaction temperature, and when the reaction temperature exceeded 300 °C, the presence of water vapor promotes the SCR performance, which is similar to previous studies [34,60]. This is due to the presence of little water at high reaction temperatures increased the Brønsted acid sites [61].

As is well known, the sulfation of the active species is the main reason for catalyst deactivation [62,63]. The sulfate species binding with the active sites would cut off the L-H reaction mechanism by the sulfation process [34,64]. As shown in Figure 6c, the SCR activity of H550 varied significantly in the range 100–250 °C under different concentrations of SO₂. In particular, the inhibition effect was found to be greater under higher concentrations of SO₂. This could be due to the formation of NH₄HSO₄ and/or (NH₄)₂SO₄, which could accumulate on the surface of the catalyst and block the active sites [65]. When the reaction temperature exceeded 300 °C, the presence of SO₂ gave a promoting effect.

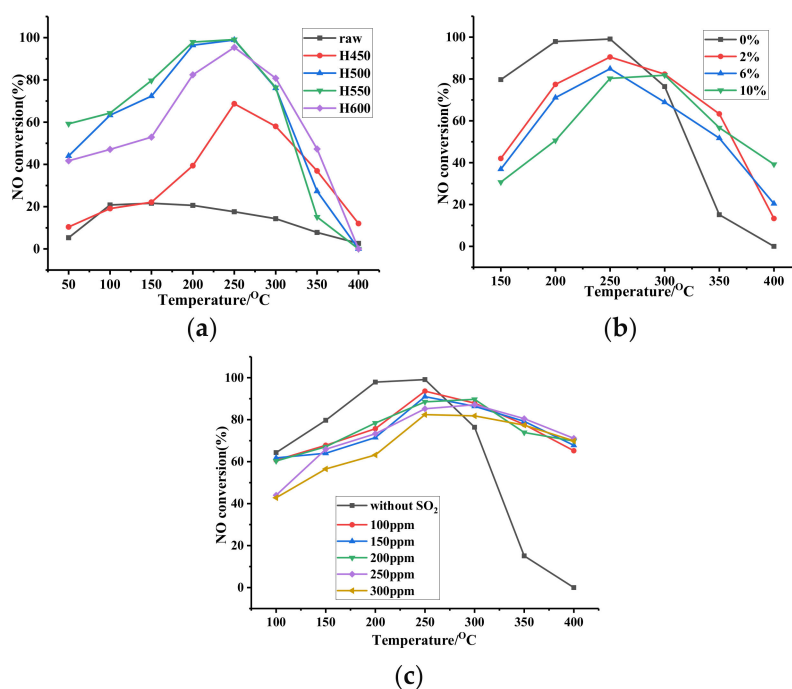


Figure 6. The NO conversion of different samples (a), H550 in the presence of water (b), and H550 in the presence of sulfur dioxide (c). (Reaction condition: NO = 500 ppm, NH₃ = 500 ppm, O₂ = 1.5 vol. %, and balance of Ar, GHSV = 16000 h⁻¹, the NO conversion of zero means the NO concentration in the outlet over the inlet).

4. Conclusions

The calcination of natural siderite at different temperatures in air atmosphere was carried out to prepare the Mn-containing α -Fe₂O₃ for NH₃-SCR. The natural siderite was gradually decomposed at 450 °C and converted into Mn-containing α -Fe₂O₃. The escape of CO₂ in the process of decomposition

of siderite improved the specific surface area. H550 had the best SCR performance with NO conversion of 98% at 200 °C, due to its larger specific surface area and nanoscale structure. In addition, with the increase of calcination temperature, the gradual conversion of Mn²⁺ into Mn⁴⁺ was responsible for the decrease of the reaction temperature window. The water and sulfur dioxide resistant experiments demonstrated that the materials have a certain resistance to water and sulfur, especially at 250 °C. Thus, this calcined siderite is an active material for NH₃-SCR reaction. The results of this study provide a new way for the utilization of natural minerals in SCR.

Author Contributions: Conceptualization, H.L., T.C. and D.C.; methodology, D.S.; formal analysis, H.L., F.S., T.C., D.S., D.C.; writing—original draft preparation, F.S.; writing—review and editing, F.S. and H.L.; supervision, H.L., T.C. and D.C.; project administration, H.L.; funding acquisition, H.L. and D.C.

Funding: This study was financially supported by the National Natural Science Foundation of China (No. 41772038, 41672040), and Anhui Provincial Natural Science Foundation (1708085MD87).

Conflicts of Interest: The authors declare no conflict of interest.

References

- Mu, J.C.; Li, X.Y.; Sun, W.B.; Fan, S.Y.; Wang, X.Y.; Wang, L.; Qin, M.C.; Gan, G.Q.; Yin, Z.F.; Zhang, D.K. Enhancement of Low-Temperature Catalytic Activity over a Highly Dispersed Fe-Mn/Ti Catalyst for Selective Catalytic Reduction of NO_x with NH₃. *Ind. Eng. Chem. Res.* **2018**, *57*, 10159–10169. [[CrossRef](#)]
- Liu, C.; Shi, J.W.; Gao, C.; Niu, C. Manganese oxide-based catalysts for low-temperature selective catalytic reduction of NO_x with NH₃: A review. *Appl. Catal. A Gen.* **2016**, *522*, 54–69. [[CrossRef](#)]
- Cheruiyot, N.K.; Wang, L.-C.; Lin, S.-L.; Yang, H.-H.; Chen, Y.-T. Effects of Selective Catalytic Reduction on the Emissions of Persistent Organic Pollutants from a Heavy-Duty Diesel Engine. *Aerosol Air Qual. Res.* **2017**, *17*, 1658–1665. [[CrossRef](#)]
- Juzsakova, T.; Al-Jammal, N.; Cretescu, I.; Sebestyen, V.; Cuong Le, P.; Domokos, E.; Redey, A.; Stan, C.D. Case Studies for Clean Technology Development in the Chemical Industry Using Zeolite Based Catalysts. *Minerals* **2018**, *8*, 462. [[CrossRef](#)]
- Yao, X.; Zhang, L.; Li, L.; Liu, L.; Cao, Y.; Dong, X.; Gao, F.; Yu, D.; Tang, C.; Chen, Z. Investigation of the structure, acidity, and catalytic performance of CuO/Ti_{0.95}Ce_{0.05}O₂ catalyst for the selective catalytic reduction of NO by NH₃ at low temperature. *Appl. Catal. B Environ.* **2014**, *150*, 315–329. [[CrossRef](#)]
- Zhang, L.; Zhang, D.; Zhang, J.; Cai, S.; Fang, C.; Huang, L.; Li, H.; Gao, R.; Shi, L. Design of meso-TiO₂@MnO(x)-CeO(x)/CNTs with a core-shell structure as DeNO(x) catalysts: Promotion of activity, stability and SO₂-tolerance. *Nanoscale* **2013**, *5*, 9821–9829. [[CrossRef](#)] [[PubMed](#)]
- Zhang, C.; Chen, T.; Liu, H.; Chen, D.; Xu, B.; Qing, C. Low temperature SCR reaction over Nano-Structured Fe-Mn Oxides: Characterization, performance, and kinetic study. *Appl. Surf. Sci.* **2018**, *457*, 1116–1125. [[CrossRef](#)]
- Liu, S.; Ji, P.; Ye, D.; Qu, R.; Zheng, C.; Gao, X. Regeneration of Potassium Poisoned Catalysts for the Selective Catalytic Reduction of NO with NH₃. *Aerosol Air Qual. Res.* **2019**, *19*, 649–656. [[CrossRef](#)]
- Schill, L.; Putluru, S.S.R.; Fehrmann, R.; Jensen, A.D. Low-Temperature NH₃-SCR of NO on Mesoporous Mn_{0.6}Fe_{0.4}/TiO₂ Prepared by a Hydrothermal Method. *Catal. Lett.* **2014**, *144*, 395–402. [[CrossRef](#)]
- Li, Q.; Liu, H.; Chen, T.; Chen, D.; Zhang, C.; Xu, B.; Zhu, C.; Jiang, Y. Characterization and SCR Performance of Nano-Structured Iron-Manganese Oxides: Effect of Annealing Temperature. *Aerosol Air Qual. Res.* **2017**, *17*, 2328–2337. [[CrossRef](#)]
- Yang, S.; Wang, C.; Ma, L.; Peng, Y.; Qu, Z.; Yan, N.; Chen, J.; Chang, H.; Li, J. Substitution of WO₃ in V₂O₅/WO₃-TiO₂ by Fe₂O₃ for selective catalytic reduction of NO with NH₃. *Catal. Sci. Technol.* **2012**, *3*, 161–168. [[CrossRef](#)]
- Liu, Z.; Zhang, S.; Li, J.; Zhu, J.; Ma, L. Novel V₂O₅-CeO₂/TiO₂ catalyst with low vanadium loading for the selective catalytic reduction of NO_x by NH₃. *Appl. Catal. B Environ.* **2014**, *158*, 11–19. [[CrossRef](#)]
- Chen, Y.; Wang, M.; Du, X.; Ran, J.; Zhang, L.; Tang, D. High Resistance to Na Poisoning of the V₂O₅-Ce(SO₄)₂/TiO₂ Catalyst for the NO SCR Reaction. *Aerosol Air Qual. Res.* **2018**, *18*, 2948–2955. [[CrossRef](#)]

14. Liu, F.; He, H. Structure–Activity Relationship of Iron Titanate Catalysts in the Selective Catalytic Reduction of NO_x with NH₃. *J. Phys. Chem. C* **2010**, *114*, 16929–16936. [[CrossRef](#)]
15. Youn, S.; Song, I.; Kim, D.H. Roles of Promoters in V₂O₅/TiO₂ Catalysts for Selective Catalytic Reduction of NO_x with NH₃: Effect of Order of Impregnation. *J. Nanosci. Nanotechnol.* **2016**, *16*, 4350–4356. [[CrossRef](#)]
16. Ma, L.; Li, J.; Ke, R.; Fu, L. Catalytic Performance, Characterization, and Mechanism Study of Fe₂(SO₄)₃/TiO₂ Catalyst for Selective Catalytic Reduction of NO_x by Ammonia. *J. Phys. Chem. C* **2011**, *115*, 7602–7603. [[CrossRef](#)]
17. Min, K.; Park, E.D.; Ji, M.K.; Yie, J.E. Manganese oxide catalysts for NO_x reduction with NH₃ at low temperatures. *Appl. Catal. A Gen.* **2007**, *327*, 261–269.
18. Chen, J.P.; Hausladen, M.C.; Yang, R.T. Delaminated Fe₂O₃-pillared clay: Its preparation, characterization, and activities for selective catalytic reduction of NO by NH₃. *J. Catal.* **1995**, *151*, 135–146. [[CrossRef](#)]
19. Putluru, S.S.R.; Schill, L.; Jensen, A.D.; Siret, B.; Tabaries, F.; Fehrmann, R. Mn/TiO₂ and Mn-Fe/TiO₂ catalysts synthesized by deposition precipitation—Promising for selective catalytic reduction of NO with NH₃ at low temperatures. *Appl. Catal. B Environ.* **2014**, *165*, 628–635. [[CrossRef](#)]
20. Liu, H.; Zhang, Z.; Li, Q.; Chen, T.; Zhang, C.; Chen, D.; Zhu, C.; Jiang, Y. Novel Method for Preparing Controllable Nanoporous α-Fe₂O₃ and its Reactivity to SCR De-NO_x. *Aerosol Air Qual. Res.* **2017**, *17*, 1898–1908. [[CrossRef](#)]
21. Bell, M.S.; Schwandt, C.S.; Zolensky, M.E.; Hörz, F. Experimental Shock Decomposition of Siderite. *Meteorit. Planet. Sci.* **2002**, *37*, 1–6.
22. Zhang, D.; Zhang, L.; Shi, L.; Fang, C.; Li, H.; Gao, R.; Huang, L.; Zhang, J. In situ supported MnO(x)-CeO(x) on carbon nanotubes for the low-temperature selective catalytic reduction of NO with NH₃. *Nanoscale* **2013**, *5*, 1127–1136. [[CrossRef](#)] [[PubMed](#)]
23. Yao, X.; Kong, T.; Yu, S.; Li, L.; Yang, F.; Dong, L. Influence of different supports on the physicochemical properties and denitration performance of the supported Mn-based catalysts for NH₃-SCR at low temperature. *Appl. Surf. Sci.* **2017**, *402*, 208–217. [[CrossRef](#)]
24. Qi, G.; Yang, R.T. Low-temperature selective catalytic reduction of NO with NH over iron and manganese oxides supported on titania. *Appl. Catal. B Environ.* **2003**, *44*, 217–225. [[CrossRef](#)]
25. Liu, D.; Zhou, A.; Zeng, F.; Zhao, F.; Zou, Y. The Petrography, Mineralogy and Geochemistry of Some Cu- and Pb-Enriched Coals from Jungar Coalfield, Northwestern China. *Minerals* **2018**, *8*, 5. [[CrossRef](#)]
26. Wang, X.; Zhang, L.; Jiang, Y.; Wei, J.; Chen, Z. Mineralogical and Geochemical Characteristics of the Early Permian Upper No. 3 Coal from Southwestern Shandong, China. *Minerals* **2016**, *6*, 58. [[CrossRef](#)]
27. Zhang, Z.; Liu, H.; Ping, L.; Chen, T.; Ma, W. Nanostructured α-Fe₂O₃ derived from siderite as an effective Hg(II) adsorbent: Performance and mechanism. *Appl. Geochem.* **2018**, *96*, 92–99. [[CrossRef](#)]
28. Liu, H.; Chen, T.; Zou, X.; Qing, C.; Frost, R.L. Thermal treatment of natural goethite: Thermal transformation and physical properties. *Thermochim. Acta* **2013**, *568*, 115–121. [[CrossRef](#)]
29. Li, M.; Sun, Y.; Liu, H.; Chen, T.; Hayat, T.; Alharbi, N.S.; Chen, C. Spectroscopic and modeling investigation of Eu(III) and U(VI) adsorption on nano-magnetite from aqueous solutions. *ACS Sustain. Chem. Eng.* **2017**, *5*, 5493–5502. [[CrossRef](#)]
30. Fan, Y.; Ling, W.; Dong, L.; Li, S.; Yu, C.; Huang, B.; Xi, H. In Situ FT-IR and DFT Study of the Synergistic Effects of Cerium Presence in the Framework and the Surface in NH₃-SCR. *Aerosol Air Qual. Res.* **2018**, *18*, 655–670. [[CrossRef](#)]
31. Luo, Y.H.; Zhu, D.Q.; Pan, J.; Zhou, X.L. Thermal decomposition behaviour and kinetics of Xinjiang siderite ore. *Miner. Process. Extr. Metall.* **2016**, *125*, 17–25. [[CrossRef](#)]
32. Zhang, X.; Han, Y.; Li, Y.; Sun, Y. Effect of Heating Rate on Pyrolysis Behavior and Kinetic Characteristics of Siderite. *Minerals* **2017**, *7*, 211. [[CrossRef](#)]
33. Zhang, W.; Shi, Y.; Li, C.; Zhao, Q.; Li, X. Synthesis of Bimetallic MOFs MIL-100(Fe-Mn) as an Efficient Catalyst for Selective Catalytic Reduction of NO_x with NH₃. *Catal. Lett.* **2016**, *146*, 1956–1964. [[CrossRef](#)]
34. Zhu, L.; Zhong, Z.; Yang, H.; Wang, C. NH₃-SCR Performance of Mn-Fe/TiO₂ Catalysts at Low Temperature in the Absence and Presence of Water Vapor. *Water Air Soil Pollut.* **2016**, *227*, 476. [[CrossRef](#)]
35. Liu, F.; He, H.; Lian, Z.; Shan, W.; Xie, L.; Asakura, K.; Yang, W.; Deng, H. Highly dispersed iron vanadate catalyst supported on TiO₂ for the selective catalytic reduction of NO_x with NH₃. *J. Catal.* **2013**, *307*, 340–351. [[CrossRef](#)]

36. Wu, S.; Zhang, L.; Wang, X.; Zou, W.; Cao, Y.; Sun, J.; Tang, C.; Gao, F.; Deng, Y.; Dong, L. Synthesis, characterization and catalytic performance of FeMnTiO_x mixed oxides catalyst prepared by a CTAB-assisted process for mid-low temperature NH₃-SCR. *Appl. Catal. A Gen.* **2015**, *505*, 235–242. [[CrossRef](#)]
37. Grosvenor, A.P.; Kobe, B.A.; Biesinger, M.C.; McIntyre, N.S. Investigation of multiplet splitting of Fe 2p XPS spectra and bonding in iron compounds. *Surf. Interface Anal.* **2004**, *36*, 1564–1574. [[CrossRef](#)]
38. Heuer, J.K.; Stubbins, J.F. An XPS characterization of FeCO₃ films from CO₂ corrosion. *Corros. Sci.* **1999**, *41*, 1231–1243. [[CrossRef](#)]
39. Devaiah, D.; Smirniotis, P.G. Role of the Ce and Cr Content of Fe-Ce-Cr Ferrite Spinel for the High Temperature Water-Gas Shift Reaction. *Ind. Eng. Chem. Res.* **2017**, *56*, 1772–1781. [[CrossRef](#)]
40. Liu, C.; Yang, S.; Ma, L.; Peng, Y.; Hamidreza, A.; Chang, H.; Li, J. Comparison on the Performance of α-Fe₂O₃ and γ-Fe₂O₃ for Selective Catalytic Reduction of Nitrogen Oxides with Ammonia. *Catal. Lett.* **2013**, *143*, 697–704. [[CrossRef](#)]
41. Zhang, L.; Shi, L.; Huang, L.; Zhang, J.; Gao, R.; Zhang, D. Rational Design of High-Performance DeNO_x Catalysts Based on MN_xCO_{3-x}O₄ Nanocages Derived from Metal–Organic Frameworks. *ACS Catal.* **2014**, *4*, 1753–1763. [[CrossRef](#)]
42. Hu, H.; Zha, K.; Li, H.; Shi, L.; Zhang, D. In situ DRIFTS investigation of the reaction mechanism over MnO_x-MO_y/Ce_{0.75}Zr_{0.25}O₂ (M = Fe, Co, Ni, Cu) for the selective catalytic reduction of NO_x with NH₃. *Appl. Surf. Sci.* **2016**, *387*, 921–928. [[CrossRef](#)]
43. Yu, J.; Guo, F.; Wang, Y.; Zhu, J.; Liu, Y.; Su, F.; Gao, S.; Xu, G. Sulfur poisoning resistant mesoporous Mn-based catalyst for low-temperature SCR of NO with NH₃. *Appl. Catal. B Environ.* **2010**, *95*, 160–168. [[CrossRef](#)]
44. Yao, X.; Li, L.; Zou, W.; Yu, S.; An, J.; Li, H.; Yang, F.; Dong, L. Preparation, characterization, and catalytic performance of high efficient CeO₂-MnO_x-Al₂O₃ catalysts for NO elimination. *Chin. J. Catal.* **2016**, *37*, 1369–1380. [[CrossRef](#)]
45. Ilton, E.S.; Post, J.E.; Heaney, P.J.; Ling, F.T.; Kerisit, S.N. XPS determination of Mn oxidation states in Mn (hydr)oxides. *Appl. Surf. Sci.* **2016**, *366*, 475–485. [[CrossRef](#)]
46. Ristić, M.; Krehula, S.; Reissner, M.; Musić, S. 57Fe Mössbauer, XRD, FT-IR, FE SEM Analyses of Natural Goethite, Hematite and Siderite. *Croat. Chem. Acta* **2017**, *90*, 499–507. [[CrossRef](#)]
47. Wu, X.; Xu, P.; Duan, Y.; Hu, C.; Li, G. Surface magnetization of siderite mineral. *Int. J. Min. Sci. Technol.* **2012**, *22*, 825–830. [[CrossRef](#)]
48. Liu, H.; Shu, D.; Sun, F.; Li, Q.; Chen, T.; Xing, B.; Chen, D.; Qing, C. Effect of manganese substitution on the crystal structure and decomposition kinetics of siderite. *J. Therm. Anal. Calorim.* **2018**, *136*, 1315–1322. [[CrossRef](#)]
49. Fang, C.; Zhang, D.; Shi, L.; Gao, R.; Li, H.; Ye, L.; Zhang, J. Highly dispersed CeO₂ on carbon nanotubes for selective catalytic reduction of NO with NH₃. *Catal. Sci. Technol.* **2013**, *3*, 803–811. [[CrossRef](#)]
50. Liu, X.L.; Guo, J.X.; Chu, Y.H.; Luo, D.M.; Yin, H.Q.; Sun, M.C.; Yavuz, R. Desulfurization performance of iron supported on activated carbon. *Fuel* **2014**, *123*, 93–100. [[CrossRef](#)]
51. Cooney, T.F.; Scott, E.R.D.; Krot, A.N.; Sharma, S.K.; Yamaguchi, A. Vibrational spectroscopic study of minerals in the Martian meteorite ALH84001. *Am. Mineral.* **1999**, *84*, 1569–1576. [[CrossRef](#)]
52. Sommer, A.J.; Bogdan, C.E.; Simpson, D.R.; Herman, R.G. Discrimination Among Carbonate Minerals by Raman Spectroscopy Using the Laser Microprobe. *Appl. Spectrosc.* **1987**, *41*, 437–440.
53. Zoppi, A.; Lofrumento, C.; Castellucci, E.M.; Migliorini, M.G. The Raman spectrum of hematite: Possible indicator for a compositional or firing distinction among Terra Sigillata wares. *Ann. Di Chim.* **2010**, *95*, 239–246. [[CrossRef](#)]
54. León, C.P.; Kador, L.; Zhang, M.; Müller, A.H.E. In situ laser-induced formation of α-Fe₂O₃ from Fe₃⁺ ions in a cylindrical core-shell polymer brush. *J. Raman Spectrosc.* **2004**, *35*, 165–169. [[CrossRef](#)]
55. Chen, H.; Wang, Y.; Lv, Y.K. Catalytic oxidation of NO over MnO₂ with different crystal structures. *RSC Adv.* **2016**, *6*, 54032–54040. [[CrossRef](#)]
56. Hong, W.J.; Iwamoto, S.; Hosokawa, S.; Wada, K.; Kanai, H.; Inoue, M. Effect of Mn content on physical properties of CeO_x-MnO_y support and BaO-CeO_x-MnO_y catalysts for direct NO decomposition. *J. Catal.* **2011**, *277*, 208–216. [[CrossRef](#)]
57. Wu, Z.; Jin, R.; Wang, H.; Liu, Y. Effect of ceria doping on SO₂ resistance of Mn/TiO₂ for selective catalytic reduction of NO with NH₃ at low temperature. *Catal. Commun.* **2009**, *10*, 935–939. [[CrossRef](#)]

58. Liu, F.; He, H. Selective catalytic reduction of NO with NH₃ over manganese substituted iron titanate catalyst: Reaction mechanism and H₂O/SO₂ inhibition mechanism study. *Catal. Today* **2010**, *153*, 70–76. [[CrossRef](#)]
59. Lian, Z.; Liu, F.; He, H.; Shi, X.; Mo, J.; Wu, Z. Manganese–niobium mixed oxide catalyst for the selective catalytic reduction of NO_x with NH₃ at low temperatures. *Chem. Eng. J.* **2014**, *250*, 390–398. [[CrossRef](#)]
60. Long, R.Q.; Yang, R.T.; Chang, R. Low temperature selective catalytic reduction (SCR) of NO with NH₃ over Fe-Mn based catalysts. *Chem. Commun.* **2002**, *5*, 452–453. [[CrossRef](#)]
61. Jiang, Y.; Gao, X.; Wu, W. Effects of H₂O and SO₂ on the Performance of V₂O₅/TiO₂ Catalysts for Selective Catalytic Reduction of NO in Flue Gas. *Proc. CSEE* **2013**, *33*, 28–33.
62. Sheng, Z.Y.; Hu, Y.F.; Xue, J.M.; Wang, X.M.; Liao, W.P. SO₂ poisoning and regeneration of Mn-Ce/TiO₂ catalyst for low temperature NO_x reduction with NH₃. *J. Rare Earths* **2012**, *30*, 676–682. [[CrossRef](#)]
63. Casapu, M.; Kröcher, O.; Elsener, M. Screening of doped MnO_x–CeO₂ catalysts for low-temperature NO-SCR. *Appl. Catal. B Environ.* **2009**, *88*, 413–419. [[CrossRef](#)]
64. Jiang, B.Q.; Wu, Z.B.; Liu, Y.; Lee, S.C.; Ho, W.K. DRIFT Study of the SO₂ Effect on Low-Temperature SCR Reaction over Fe–Mn/TiO₂. *J. Phys. Chem. C* **2010**, *114*, 4961–4965. [[CrossRef](#)]
65. Jiang, Y.; Wang, X.; Xing, Z.; Bao, C.; Liang, G. Preparation and Characterization of CeO₂-MoO₃/TiO₂ Catalysts for Selective Catalytic Reduction of NO with NH₃. *Aerosol Air Qual. Res.* **2017**, *17*, 2726–2734. [[CrossRef](#)]



© 2019 by the authors. Licensee MDPI, Basel, Switzerland. This article is an open access article distributed under the terms and conditions of the Creative Commons Attribution (CC BY) license (<http://creativecommons.org/licenses/by/4.0/>).